NUMERICAL METHODS FOR THE PHOTOELASTIC TECHNIQUE USING PHASE SHIFTING

C. A. Magalhaes

Coordenacoes das Engenharias
Centro Universitario Newton Paiva
Belo Horizonte, Brazil

Departamento de Engenharia Mecanica
Pontifícia Universidade Católica de Minas Gerais
Belo Horizonte, Brazil

P. S. Neto **P. A. A. Magalhaes Jr.***

Departamento de Engenharia Mecanica
Pontifícia Universidade Católica de Minas Gerais
Belo Horizonte, Brazil

C. S. de Barcellos

Departamento de Engenharia Mecanica
Univesidade Federal de Santa Catarina
Florianópolis, Brazil

ABSTRACT

The objective of this research is to find new equations for a novel phase-shifting method in digital photoelasticity. Some innovations are proposed. In terms of phase-shifting, only the analyzer is rotated, and the other equations are deduced by applying a new numerical technique instead of the usual algebraic techniques. This approach can be used to calculate a larger sequence of images. Each image represents a pattern and a measurement of the stresses present in the object. A reduction in the difference between the theoretical and experimental values of stresses was obtained by increasing the number of images in the equations for calculating phase. Every photographic image has errors and random noise, but the uncertainties due to these effects can be reduced with a larger number of observations.

Keywords: Photoelasticity, Phase shifting, Numerical methods, Stress measurement.

1. INTRODUCTION

Photoelasticity is one of the oldest methods for experimental stress analysis, but it has been overshadowed by the Finite Element Method for engineering applications over the past two to three decades. However, certain new and novel developments and applications have revived the use of photoelasticity. The new approach involves the use of hybrid methods in which the advantages of both experimental and numerical methods are exploited. Nevertheless, recent industrial needs, such as the continuous on-line monitoring of structures, determination of the residual stresses in glass (plastics) and microelectronics materials, rapid prototype production and dynamic visualization of stress waves, have brought photoelasticity into the limelight once again [1].

The current trend of digitally imaging photoelastic fringe patterns indicates that image processing can be used to delineate the required information from the fringe patterns. The phase-shifting method has the most potential, particularly with respect to fringe sign determination. The method of photoelasticity makes it possible to obtain the principal stress directions and principal stress differences in a model. The principal stress directions and the principal stress differences are provided by isoclinics and isochromatics, respectively [2]. Isoclinics are the loci of the points in the specimen along which the principal stresses lie in the same direction. Isochromatics are the loci of the points along which the difference in the first and second principal stress remains the same. Thus, they are the lines that join the points with equal maximum shear stress magnitudes [3].

The fringe patterns are nothing but the record of the phase difference between light travelling in two different optical paths as intensity variations. By varying the phase difference between the beams involved, in known steps, it is possible to generate a sufficient number of equations to solve the parameters involved. In general, phase differences can be added by altering the optical path length of any one of the light beams. Usually, the phase of the reference light beam is altered in known steps. Photoelasticity falls into a special category, in that the two light beams cannot be treated separately, but rather always go together [4]. This means a phase shift introduced in one light beam will also introduce a corresponding phase shift in the other beam. This change in phase, in practice, is achieved by appropriately rotating the optical elements of the polariscope. A detailed study of the intensity of the light transmitted can help in relating the rotation of the optical elements to the change in phase introduced [5].

The significant advantage of the methodology pro-

* Corresponding author (pamerico@pucminas.br)

DOI : 10.1017/jmech.2015.20
Copyright © 2015 The Society of Theoretical and Applied Mechanics, R.O.C.
https://doi.org/10.1017/jmech.2015.20 Published online by Cambridge University Press

posed in this paper is that the method only changes the angle of the analyzer in the circular polariscope and that one can obtain equations for calculating the phase for any number of images in various situations. A clearer physical reason for the proposed numerical model is the measurement uncertainty can be reduced by increasing the number of observations. Measurement uncertainty is a parameter characterizing the dispersion of the values attributed to a measured quantity. No measurement is exact. The uncertainty has a probabilistic basis and reflects incomplete knowledge of the quantity. All measurements are subject to uncertainty and a measured value is only complete if it is accompanied by a statement of the associated uncertainty. The new method can be used with any number of photographic images or photoelastic measures in plane or circular polariscope [6].

2. PHASE-SHIFTING METHODS OF ANALYSIS

The optical arrangement to recognize and to identify isoclinics and isochromatics from photoelastic fringes is a circular polariscope set-up, shown in Fig. 1. In Fig. 1, P, Q, R, and A represent the polarizer, quarter-wave plate, retarder (stressed model) and analyzer, respectively. The orientation of the element is written by a subscript, which means the angle between the polarizing axis and the horizontal x axis. $R_{\alpha,\delta}$ represents the stressed sample taken as a retardation δ and whose fast axis is at an angle α with the x axis [7]. Therefore, $P_{90}Q_{45}R_{\alpha,\delta}Q_{-45}A_{\theta}$, indicates the following: A polarizer at 90°, a quarter -wave plate with a fast axis at 45°, a specimen as retardation δ whose fast axis is at an angle α with the x axis, a quarter-wave plate with a fast axis at −45°, and an analyzer at θ. With the Jones calculus [8] for the arrangement of $P_{90}Q_{45}R_{\alpha,\delta}Q_{-45}A_{\theta}$ shown in Fig. 1, the components of the electric field in light along and perpendicular to the analyzer axis (E_x, E_y) are given as

$$\begin{pmatrix} E_x \\ E_y \end{pmatrix} = \begin{bmatrix} \cos^2\theta & \sin\theta\cos\theta \\ \sin\theta\cos\theta & \sin^2\theta \end{bmatrix} \times \begin{bmatrix} 1+i & 1-i \\ 1-i & 1+i \end{bmatrix} \times \begin{bmatrix} e^{i\delta}\cos^2\alpha+\sin^2\alpha & (e^{i\delta}-1)\sin\alpha\cos\alpha \\ (e^{i\delta}-1)\sin\alpha\cos\alpha & e^{i\delta}\sin^2\alpha+\cos^2\alpha \end{bmatrix} \times \left(\frac{i+1}{4}\right)\begin{bmatrix} 1 & i \\ i & 1 \end{bmatrix}\begin{pmatrix} 0 \\ 1 \end{pmatrix} ke^{iwt} \quad (1)$$

where $i=\sqrt{-1}$. The angles, θ and $\varphi=-45°$ are that of the analyzer and the second quarter-wave plate form with the reference x axis, respectively. The symbols k and ω are the amplitude and the angular frequency of the light vector, respectively.

$$I = \overline{E_x}E_x + \overline{E_y}E_y \quad (2)$$

In Eq. (2), I is the output light intensity, and $\overline{E_x}$ and $\overline{E_y}$ are the complex conjugate of E_x and E_y, respectively. After the simple operation of Eq. (1) by Eq. (2), the output intensity of the circular polariscope for the arrangement $P_{90}Q_{45}R_{\alpha,\delta}Q_{-45}A_{\theta}$ is given by

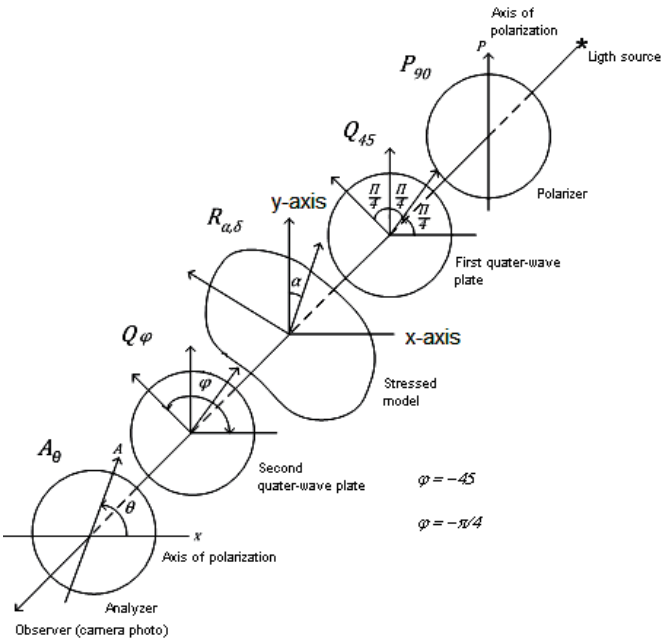


Fig. 1 Optical arrangement of a circular polariscope (180° = π radians). In the figure have the coordinate system where the x axis horizontal and the vertical y-axis.

$$I = K\left[1-\cos(2\theta)\cos(\delta)-\cos(2\alpha)\sin(2\theta)\sin(\delta)\right] \quad (3)$$

where K is a proportional constant, *i.e.* the maximum light intensity emerging from the analyzer. These angle values (the polarizer with 90°, the first quarter-wave plate with 45° and the second quarter-wave plate with −45°) are chosen to simplify the calibration of the polariscope used in the experiments measurements. For the phase measuring technique, the angle α and the relative retardation δ indicating the direction and the difference of principal stresses, respectively, are the parameters to be obtained.

In the experiments, Fig. 2, the diameter and the thickness of the disk used are D = 10.0cm and H = 0.5cm, respectively. A diametrical compression load, P = 50.0N, is applied to the disk. The material fringe constant F = 900.00N/m is used. From the given conditions, the theoretical value of isochromatic δ is related to two principal stress components, σ_1 and σ_2, as in Eq. (4). In contrast, the theoretical isocline angle α can be calculated by Eq. (5) using stress components σ_x, σ_y, and τ_{xy} [7].

$$\delta = \frac{2\pi H}{F}(\sigma_1-\sigma_2) \quad (4)$$

$$\alpha = \frac{1}{2}\tan^{-1}\left(\frac{2\tau_{xy}}{\sigma_x-\sigma_y}\right) \quad (5)$$

In the literature on the theory of elasticity [9,10], the exact value of the stress field, as a function of x and y with its origin at the center of the disc, is given by (the superscript "e" indicates the exact, analytical values):

https://doi.org/10.1017/jmech.2015.20 Published online by Cambridge University Press

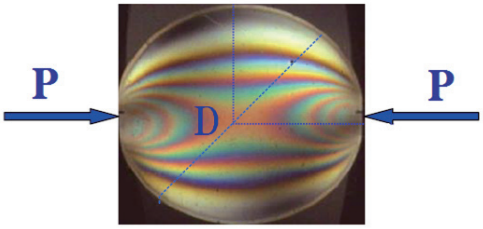


Fig. 2 Sample under compression.

$$\sigma_x^e = \frac{-2P}{\pi H}\left\{\frac{(D/2-y)x^2}{\left[x^2+(D/2-y)^2\right]^2}+\frac{(D/2+y)x^2}{\left[x^2+(D/2+y)^2\right]^2}-\frac{1}{D}\right\} \tag{6}$$

$$\sigma_y^e = \frac{-2P}{\pi H}\left\{\frac{(D/2-y)^3}{\left[x^2+(D/2-y)^2\right]^2}+\frac{(D/2+y)^3}{\left[x^2+(D/2+y)^2\right]^2}-\frac{1}{D}\right\} \tag{7}$$

$$\tau_{xy}^e = \frac{2P}{\pi H}\left\{\frac{(D/2-y)^2 x}{\left[x^2+(D/2-y)^2\right]^2}+\frac{(D/2+y)^2 x}{\left[x^2+(D/2+y)^2\right]^2}\right\} \tag{8}$$

For comparison with the experimentally measured values, the following are used:

$$\sigma_1^e = \frac{(\sigma_x^e+\sigma_y^e)}{2}-\sqrt{\frac{1}{4}(\sigma_x^e-\sigma_y^e)^2+(\tau_{xy}^e)^2} \tag{9}$$

$$\sigma_2^e = \frac{(\sigma_x^e+\sigma_y^e)}{2}+\sqrt{\frac{1}{4}(\sigma_x^e-\sigma_y^e)^2+(\tau_{xy}^e)^2} \tag{10}$$

Then, with Eqs. (11) and (12), the exact values of δ^e and α^e can to be calculated for each point of the x and y coordinates in the same manner as in Eqs. (4) and (5):

$$\delta^e = \frac{2\pi H}{F}(\sigma_1^e-\sigma_2^e) \tag{11}$$

$$\alpha^e = \frac{1}{2}\tan^{-1}\left(\frac{2\tau_{xy}^e}{\sigma_x^e-\sigma_y^e}\right) \tag{12}$$

Figures 3, and 4 show the result of applying the analytical Eqs. 11 and 12. The idea is to compare these exact results (δ^e and α^e) obtained theoretically in the analysis of stress with experimental measurements of light intensities using the proposed method (δ and α).

3. NEW MATHEMATICAL MODEL

By analogy with the equations of phase calculation used by other authors and the mathematical model proposed in [11]. We had the idea to try a new general model for the equations of phase in photoelasticity. After many different attempts, a general equation for calculating the phase for any number, N, of images is proposed:

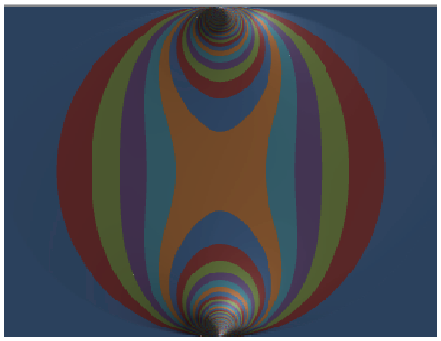


Fig. 3 Analytical solution of δ^e for a disc on compression, using Eq. (11). The color change over a range of 2π radians in order to simulate the formation of fringes (Phase maps of isochromatics).

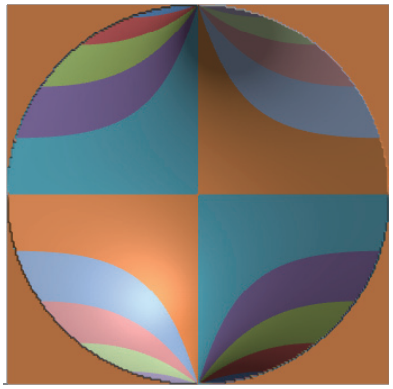


Fig. 4 Analytical solution of α^e for a disc on compression, using Eq. (12). The color change over a range of 0.3 radians in order to simulate the formation of fringes (Phase maps of isoclinics).

$$\alpha = \frac{1}{2}\tan^{-1}\left(\frac{\sqrt{\left|\sum_{r=1}^{N}\sum_{s=r}^{N} b_{r,s}\, I_r\, I_s\right|}}{\sqrt{\left|\sum_{r=1}^{N}\sum_{s=r}^{N} c_{r,s}\, I_r\, I_s\right|}}\right) \tag{13}$$

$$\delta = \tan^{-1}\left(\frac{\sqrt{\left|\sum_{r=1}^{N}\sum_{s=r}^{N} e_{r,s}\, I_r\, I_s\right|}}{\sqrt{\left|\sum_{r=1}^{N}\sum_{s=r}^{N} f_{r,s}\, I_r\, I_s\right|}}\right) \tag{14}$$

where N is the number of images, $b_{r,s}$ and $e_{r,s}$ are coefficients of the numerator, $c_{r,s}$ and $f_{r,s}$ are coefficients of the denominator, and r and s are the index of the sum [11], as same model of equation. Expanding the summations and allowing an arbitrary number of lines yields

https://doi.org/10.1017/jmech.2015.20 Published online by Cambridge University Press

$$\alpha = \frac{1}{2}\tan^{-1}\left(\frac{\sqrt{\begin{vmatrix} b_{1,1}I_1^2 & +b_{1,2}I_1I_2 & +b_{1,3}I_1I_3 & +b_{1,4}I_1I_4 & \dots & +b_{1,N}I_1I_N \\ & +b_{2,2}I_2^2 & +b_{2,3}I_2I_3 & +b_{2,4}I_2I_4 & \dots & +b_{2,N}I_2I_N \\ & & +b_{3,3}I_3^2 & +b_{3,4}I_3I_4 & \dots & +b_{3,N}I_3I_N \\ & & & +b_{4,4}I_4^2 & \dots & +b_{4,N}I_4I_N \\ & & & & \dots & \dots \\ & & & & & +b_{N,N}I_N^2 \end{vmatrix}}}{\sqrt{\begin{vmatrix} c_{1,1}I_1^2 & +c_{1,2}I_1I_2 & +c_{1,3}I_1I_3 & +c_{1,4}I_1I_4 & \dots & +c_{1,N}I_1I_N \\ & +c_{2,2}I_2^2 & +c_{2,3}I_2I_3 & +c_{2,4}I_2I_4 & \dots & +c_{2,N}I_2I_N \\ & & +c_{3,3}I_3^2 & +c_{3,4}I_3I_4 & \dots & +c_{3,N}I_3I_N \\ & & & +c_{4,4}I_4^2 & \dots & +c_{4,N}I_4I_N \\ & & & & \dots & \dots \\ & & & & & +c_{N,N}I_N^2 \end{vmatrix}}}\right) \tag{15}$$

$$\delta = \tan^{-1}\left(\frac{\sqrt{\begin{vmatrix} e_{1,1}I_1^2 & +e_{1,2}I_1I_2 & +e_{1,3}I_1I_3 & +e_{1,4}I_1I_4 & \dots & +e_{1,N}I_1I_N \\ & +e_{2,2}I_2^2 & +e_{2,3}I_2I_3 & +e_{2,4}I_2I_4 & \dots & +e_{2,N}I_2I_N \\ & & +e_{3,3}I_3^2 & +e_{3,4}I_3I_4 & \dots & +e_{3,N}I_3I_N \\ & & & +e_{4,4}I_4^2 & \dots & +e_{4,N}I_4I_N \\ & & & & \dots & \dots \\ & & & & & +e_{N,N}I_N^2 \end{vmatrix}}}{\sqrt{\begin{vmatrix} f_{1,1}I_1^2 & +f_{1,2}I_1I_2 & +f_{1,3}I_1I_3 & +f_{1,4}I_1I_4 & \dots & +f_{1,N}I_1I_N \\ & +f_{2,2}I_2^2 & +f_{2,3}I_2I_3 & +f_{2,4}I_2I_4 & \dots & +f_{2,N}I_2I_N \\ & & +f_{3,3}I_3^2 & +f_{3,4}I_3I_4 & \dots & +f_{3,N}I_3I_N \\ & & & +f_{4,4}I_4^2 & \dots & +f_{4,N}I_4I_N \\ & & & & \dots & \dots \\ & & & & & +f_{N,N}I_N^2 \end{vmatrix}}}\right) \tag{16}$$

In contrast, emphasizing only the matrix of coefficients of the numerator and the denominator:

$$\alpha = \frac{1}{2}\tan^{-1}\frac{\sqrt{|\,Num_\alpha\,|}}{\sqrt{|\,Den_\alpha\,|}} \begin{cases} Num_\alpha = \begin{bmatrix} b_{1,1} & b_{1,2} & b_{1,3} & b_{1,4} & \dots & b_{1,N} \\ & b_{2,2} & b_{2,3} & b_{2,4} & \dots & b_{2,N} \\ & & b_{3,3} & b_{3,4} & \dots & b_{3,N} \\ & & & b_{4,4} & \dots & b_{4,N} \\ & & & & \dots & \dots \\ & & & & & b_{N,N} \end{bmatrix} \\ Den_\alpha = \begin{bmatrix} c_{1,1} & c_{1,2} & c_{1,3} & c_{1,4} & \dots & c_{1,N} \\ & c_{2,2} & c_{2,3} & c_{2,4} & \dots & c_{2,N} \\ & & c_{3,3} & c_{3,4} & \dots & c_{3,N} \\ & & & c_{4,4} & \dots & c_{4,N} \\ & & & & \dots & \dots \\ & & & & & c_{N,N} \end{bmatrix} \end{cases} \tag{17}$$

https://doi.org/10.1017/jmech.2015.20 Published online by Cambridge University Press

$$\delta = \tan^{-1}\frac{\sqrt{|\,Num_\delta\,|}}{\sqrt{|\,Den_\delta\,|}}\begin{cases} Num_\delta = \begin{bmatrix} e_{1,1} & e_{1,2} & e_{1,3} & e_{1,4} & \cdots & e_{1,N} \\ & e_{2,2} & e_{2,3} & e_{2,4} & \cdots & e_{2,N} \\ & & e_{3,3} & e_{3,4} & \cdots & e_{3,N} \\ & & & e_{4,4} & \cdots & e_{4,N} \\ & & & & \cdots & \cdots \\ & & & & & e_{N,N} \end{bmatrix} \\ Den_\delta = \begin{bmatrix} f_{1,1} & f_{1,2} & f_{1,3} & f_{1,4} & \cdots & f_{1,N} \\ & f_{2,2} & f_{2,3} & f_{2,4} & \cdots & f_{2,N} \\ & & f_{3,3} & f_{3,4} & \cdots & f_{3,N} \\ & & & f_{4,4} & \cdots & f_{4,N} \\ & & & & \cdots & \cdots \\ & & & & & f_{N,N} \end{bmatrix} \end{cases} \tag{18}$$

The display of the phase calculation equation in this way permits the viewing of symmetries and the sparse matrix. The use of the absolute value in the numerator and the denominator restricts the angle between 0 and $\pi/2$ radians but avoids negative roots and also eliminates false angles. Subsequent considerations will later remove this restriction.

The shift from obtaining equations for calculating the phase analytically to obtaining them numerically is a significant innovation. It breaks a paradigm that was hitherto used by several authors. After several attempts at numerical modeling of the problem, the following mathematical problem was identified (Eq. (19)):

$$\text{Maximize} \quad \sum_{r=1}^{N}\sum_{s=r}^{N}(b_{r,s}+c_{r,s}+e_{r,s}+f_{r,s}) \tag{19}$$

Output with the real coefficients: $b_{r,s}$, $c_{r,s}$, $e_{r,s}$, $f_{r,s}$, $r = 1\ \ldots N$, $s = r \ldots N$

Subject to

$$\begin{cases} \qquad \tan(\text{angle}) = \text{Sqrt}(|\text{Num}|)/\text{Sqrt}(|\text{Den}|) & \text{Quantities} \\ 1) \quad \tan^2(2\alpha^{\nu})\left(\sum_{r=1}^{N}\sum_{s=r}^{N}(c_{r,s}I_r^{\nu}I_s^{\nu})\right) = \sum_{r=1}^{N}\sum_{s=r}^{N}(b_{r,s}I_r^{\nu}I_s^{\nu}) & \nu = 1..\left[N(N+1)\right] \\ 2) \quad \tan^2(\delta^{\nu})\left(\sum_{r=1}^{N}\sum_{s=r}^{N}(f_{r,s}I_r^{\nu}I_s^{\nu})\right) = \sum_{r=1}^{N}\sum_{s=r}^{N}(e_{r,s}I_r^{\nu}I_s^{\nu}) & \nu = 1..\left[N(N+1)\right] \\ \qquad -1 \le b_{r,s} \le 1, \quad -1 \le c_{r,s} \le 1 & r = 1..N, s = r..N \\ 3) \qquad -1 \le e_{r,s} \le 1, \quad -1 \le f_{r,s} \le 1 & r = 1..N, s = r..N \\ \qquad b_{r,s}, \ \mathrm{c}_{r,s} \text{ are real numbers} & r = 1..N, s = r..N \\ 4) \qquad e_{r,s}, \ \mathrm{f}_{r,s} \text{ are real numbers} & r = 1..N, s = r..N \end{cases}$$

where for each v:

$$\begin{cases} I_j^{\nu} = K^{\nu}\left[1-\cos(2\theta_j)\cos(\delta^{\nu})-\cos(2\alpha^{\nu})\sin(2\theta_j)\sin(\delta^{\nu})\right], \ j = 1..N \\ K^{\nu} \in [0;\ 255] \quad \text{random and real} \\ \alpha^{\nu} \in [0;\ \pi/4] \quad \text{random and real} \\ \delta^{\nu} \in [0;\ \pi/2] \quad \text{random and real} \\ \theta_j = \dfrac{\pi}{2}\left(\dfrac{j-1}{Step-1}\right)-\dfrac{\pi}{4}, j = 1..N, \ \theta_j \in \left[-\pi/4, \pi/4\right] \\ \Delta\theta = \dfrac{\pi}{2(Step-1)} \text{ radians} \end{cases}$$

Input with the integer values: $Step \ge 3$ and $N \in [3, Step]$

https://doi.org/10.1017/jmech.2015.20 Published online by Cambridge University Press

The motivation for choosing this mathematical model is the success achieved in [11] with a similar model. The idea of the mathematical model is to maximize the coefficients ($b_{r,s}$, $c_{r,s}$, $e_{r,s}$, $f_{r,s}$) so that their values are large enough (not close to zero) to make them significant in the equation obtained. *Step* represents integer values greater than or equal to 3. N is the number of images, and it is an integer number between 3 and the value of *Step*.

The constraints 1 and 2 are made so that the coefficients ($b_{r,s}$, $c_{r,s}$, $e_{r,s}$, $f_{r,s}$) generate correct values for the calculation of α and δ. To ensure that one has a hyperrestricted problem, it is suggested that the number of greater restrictions must be at least equal to the number of variables.

The constraints 3 and 4 are placed on the coefficients ($b_{r,s}$, $c_{r,s}$, $e_{r,s}$, $f_{r,s}$) that are not greater than one and are not smaller than negative one, to avoid error propagation. For the needs evaluation phase, these limiting factors will increase the values of the intensity of the observations (I) that contains errors due to noise in the observations and excellent discretization in pixels and in shades of gray.

The ν restrictions in the model are obtained by a random choice of values for K (constant proportion of the maximum intensity of light emerging from the analyzer), δ (delay in the model given by the photoelastic isochromatic fringes) and α (angle between the direction and the axis of σ_1 horizontal reference). In fact, the values of K, δ, and α can be any real number, but to maintain compatibility with the problem, we chose to limit K between 0 and 255 so that the values of I are between 0 and 255. In addition, α is limited between 0 and π/4 radians and δ between 0 and π/2 radians so that the tangents have positive values.

The angle θ is limited to −π/4 and π/4 radians and is equally spaced when *Step* = N. For other values of *Step*, the angle θ starts with a value of −π/4 and is equally spaced, but it does not reach π/4. The choice of these angles is made based on the ease of calibration in the polariscope used. Other values for the angles can be used in the mathematical model.

Step must to be an integer number. The number of images (N) should range from 3 to the value of *Step*. *Step* is used to vary the angle with constant spacing in the polariscope analyzer. For example, for 8 images (N = 8) and *Step* = 10, the angles of the analyzer polariscope (θ) are as follows: −45°, −35°, −25°, −15°, −5°, 5°, 15°, and 25°.

The mathematical model is easy to solve because it involves linear programming and a maximum global solution can be obtained using the Simplex method. The processing time for the solution of this mathematical model is very fast, a few seconds on personal computers.

For example, when N = 3 and *Step* = 3, the angles of the polariscope analyzer (θ) are −45°, 0°, and 45°. The equations obtained with the mathematical model are shown in Eqs. (20) and (21).

$$\alpha = \frac{1}{2}\tan^{-1}\left(\frac{\sqrt{\begin{vmatrix} -0.25I_1^2 & +I_1I_2 & +0.5I_1I_3 \\ & -I_2^2 & +I_2I_3 \\ & & -0.25I_3^2 \end{vmatrix}}}{\sqrt{\begin{vmatrix} 0.25I_1^2 & -0.5I_1I_3 \\ & +0.25I_3^2 \end{vmatrix}}}\right) \tag{20}$$

$$\delta = \tan^{-1}\left(\frac{\sqrt{\begin{vmatrix} I_1I_2 & \\ -I_2^2 & +I_2I_3 \end{vmatrix}}}{\sqrt{\begin{vmatrix} 0.25I_1^2 & -I_1I_2 & +0.5I_1I_3 \\ & +I_2^2 & -I_2I_3 \\ & & +0.25I_3^2 \end{vmatrix}}}\right) \tag{21}$$

In another example, when N = 4 and *Step* = 4, the angles of the polariscope analyzer (θ) are −45°, −15°, 15°, and 45°. The equations obtained with the mathematical model are shown in Eqs. (22) and (23).

$$\alpha = \frac{1}{2}\tan^{-1}\left(\frac{\sqrt{\begin{vmatrix} -0.375I_1^2 & +I_1I_2 & +I_1I_3 & +0.25I_1I_4 \\ & -I_2^2 & & +I_2I_4 \\ & & -I_3^2 & +I_3I_4 \\ & & & -0.375I_4^2 \end{vmatrix}}}{\sqrt{\begin{vmatrix} -0.25I_1^2 & +I_1I_2 & -I_1I_3 & +0.5I_1I_4 \\ & +0.5I_2^2 & -I_2I_3 & -I_2I_4 \\ & & +0.5I_3^2 & +I_3I_4 \\ & & & -0.25I_4^2 \end{vmatrix}}}\right) \tag{22}$$

$$\delta = \tan^{-1}\left(\frac{\sqrt{\begin{vmatrix} -0.125I_1^2 & +I_1I_2 & +I_1I_3 & -0.25I_1I_4 \\ & -0.5I_2^2 & -I_2I_3 & +I_2I_4 \\ & & -0.5I_3^2 & +I_3I_4 \\ & & & -0.125I_4^2 \end{vmatrix}}}{\sqrt{\begin{vmatrix} 0.5I_1^2 & -I_1I_2 & -I_1I_3 & +I_1I_4 \\ & +0.5I_2^2 & +I_2I_3 & -I_2I_4 \\ & & +0.5I_3^2 & -I_3I_4 \\ & & & +0.5I_4^2 \end{vmatrix}}}\right) \tag{23}$$

In another example, when N = 3 and *Step* = 4, the angles of the polariscope analyzer (θ) are −45°, −15°, and 15°. The equations obtained with the mathematical model are shown in Eqs. (24) and (25).

https://doi.org/10.1017/jmech.2015.20 Published online by Cambridge University Press

$$\alpha = \frac{1}{2}\tan^{-1}\left(\frac{\sqrt{\begin{vmatrix} -(1/9)I_1^2 & +(2/3)I_1I_2 & +(2/9)I_1I_3 \\ & -I_2^2 & +(2/3)I_2I_3 \\ & & -(1/9)I_3^2 \end{vmatrix}}}{\sqrt{\begin{vmatrix} +(1/3)I_2^2 & -(2/3)I_2I_3 \\ & +(1/3)I_3^2 \end{vmatrix}}}\right) \tag{24}$$

$$\delta = \tan^{-1}\left(\frac{\sqrt{\begin{vmatrix} -(5/6)I_1^2 & +(1/2)I_1I_2 & +(1/6)I_1I_3 \\ & -(1/2)I_2^2 & \\ & & +(1/6)I_3^2 \end{vmatrix}}}{\sqrt{\begin{vmatrix} (1/3)I_1^2 & -I_1I_2 & +(1/3)I_1I_3 \\ & +(3/4)I_2^2 & -(1/2)I_2I_3 \\ & & +(5/6)I_3^2 \end{vmatrix}}}\right) \tag{25}$$

In another different example, when $N = 6$ and *Step* = 6, the angles of the polariscope analyzer (θ) are –45°, –27°, –9°, 9°, 27°, and 45°. Here the differences are in coefficients be integers instead of real, this was done by changing the mathematical model for integer programming. The equations obtained with the mathematical model are shown in Eqs. (26) and (27).

$$\alpha = \frac{1}{2}\tan^{-1}\left(\frac{\sqrt{\begin{vmatrix} -2I_1^2 & +2I_1I_2 & +2I_1I_3 & +2I_1I_4 & +2I_1I_5 & +I_1I_6 \\ & -I_2^2 & & & -2I_2I_5 & +2I_2I_6 \\ & & -I_3^2 & -2I_3I_4 & & +2I_3I_6 \\ & & & -I_4^2 & & +2I_4I_6 \\ & & & & -I_5^2 & +2I_5I_6 \\ & & & & & -2I_6^2 \end{vmatrix}}}{\sqrt{\begin{vmatrix} I_1^2 & +2I_1I_2 & -I_1I_3 & +I_1I_4 & -2I_1I_5 & -2I_1I_6 \\ & -I_2^2 & -2I_2I_3 & +2I_2I_4 & +2I_2I_5 & -2I_2I_6 \\ & & +I_3^2 & -2I_3I_4 & +2I_3I_5 & +I_3I_6 \\ & & & +I_4^2 & -2I_4I_5 & -I_4I_6 \\ & & & & -I_5^2 & +2I_5I_6 \\ & & & & & +I_6^2 \end{vmatrix}}}\right) \tag{26}$$

$$\delta = \tan^{-1}\left(\frac{\sqrt{\begin{vmatrix} 2I_1I_2 & +2I_1I_3 & +2I_1I_4 & +2I_1I_5 & -3I_1I_6 \\ -2I_2^2 & & & & +2I_2I_6 \\ & -2I_3^2 & & & +2I_3I_6 \\ & & -2I_4^2 & & +2I_4I_6 \\ & & & -2I_5^2 & +2I_5I_6 \end{vmatrix}}}{\sqrt{\begin{vmatrix} 2I_1^2 & -2I_1I_2 & -2I_1I_3 & -2I_1I_4 & -2I_1I_5 & +4I_1I_6 \\ & +I_2^2 & & & +2I_2I_5 & -2I_2I_6 \\ & & +I_3^2 & +2I_3I_4 & & -2I_3I_6 \\ & & & +I_4^2 & & -2I_4I_6 \\ & & & & +I_5^2 & -2I_5I_6 \\ & & & & & +2I_6^2 \end{vmatrix}}}\right) \tag{27}$$

In another different example, when $N = 7$ and *Step* = 7, the angles of the polariscope analyzer (θ) are –45°, –30°, –15°, 0°, 15°, 30°, and 45°. The equations obtained with the mathematical model are shown in Eqs. (28) and (29). Apparently, there is no advantage in using integer coefficients in the equations for experimental measurements of stress.

https://doi.org/10.1017/jmech.2015.20 Published online by Cambridge University Press

$$\alpha = \frac{1}{2}\tan^{-1}\left(\frac{\begin{vmatrix} -2I_1^2 & +2I_1I_3 & +2I_1I_4 & +2I_1I_5 & & +2I_1I_7 \\ & +I_2^2 & +I_2I_3 & -I_2I_4 & +I_2I_5 & +I_2I_6 & \\ & & -2I_3^2 & -I_3I_4 & -I_3I_5 & +I_3I_6 & +2I_3I_7 \\ & & & -2I_4^2 & -I_4I_5 & -I_4I_6 & +2I_4I_7 \\ & & & & -2I_5^2 & +I_5I_6 & +2I_5I_7 \\ & & & & & +I_6^2 & \\ & & & & & & -2I_7^2 \end{vmatrix}}{\begin{vmatrix} I_1^2 & -I_1I_3 & +2I_1I_4 & -I_1I_5 & & -I_1I_7 \\ & & & & -2I_2I_6 & \\ & +2I_3^2 & & -2I_3I_5 & & -I_3I_7 \\ & & -I_4^2 & & & +2I_4I_7 \\ & & & +2I_5^2 & & -I_5I_7 \\ & & & & & \\ & & & & & +I_7^2 \end{vmatrix}}\right) \tag{28}$$

$$\delta = \tan^{-1}\left(\frac{\begin{vmatrix} -2I_1^2 & +2I_1I_2 & +2I_1I_3 & & +2I_1I_5 & +2I_1I_6 & -2I_1I_7 \\ & +2I_2^2 & & -2I_2I_4 & & & +2I_2I_7 \\ & & -2I_3^2 & & & & +2I_3I_7 \\ & & & -I_4^2 & & -2I_4I_6 & \\ & & & & -2I_5^2 & & +2I_5I_7 \\ & & & & & +2I_6^2 & +2I_6I_7 \\ & & & & & & -2I_7^2 \end{vmatrix}}{\begin{vmatrix} 2I_1^2 & & -2I_1I_3 & -2I_1I_4 & -2I_1I_5 & & +2I_1I_7 \\ & -I_2^2 & & & & +2I_2I_6 & \\ & & +2I_3^2 & & & & -2I_3I_7 \\ & & & +2I_4^2 & & & -2I_4I_7 \\ & & & & +2I_5^2 & & -2I_5I_7 \\ & & & & & -I_6^2 & \\ & & & & & & +2I_7^2 \end{vmatrix}}\right) \tag{29}$$

Thus, for each value of *Step* greater than or equal to 3 and N between 3 and the value of *Step*, the mathematical model Eq. (19) provides values of the real coefficients ($b_{r,s}$, $c_{r,s}$, $e_{r,s}$, $f_{r,s}$), which represents an unprecedented and new phase equation for α and δ.

Because the new equations were developed from the algorithms, a numerical calculation, rather than an analytical demonstration of trigonometric relations, is necessary to check them. It is believed that a large number of numerical tests can validate or verify these new equations or at least minimize the chance of these equations being wrong or false. To test the usefulness of the new equations for calculating the phase, a computer program was created that generated random values of $K \in [0, 255]$, $\alpha' \in [0, \pi/4]$, and $\delta' \in [0, \pi/2]$. Using Eq. (3), the program calculates N values of I_j, one for each value of θ_j. With the values of I_j, the new phase equations were applied and tested to determine whether they produced the correct values of α and δ. The values of I_j (luminous intensity of the image) are calculated with j ranging from 1 to N. The new equations with the values of I_j are applied, giving a tan (α) and a tan (δ) that must be compared with the value of randomly assigned (α' and δ') values. This comparison involves the accuracy of a very small value because of the number of rounding errors that can occur in the calculations, that is, the precision $(|\alpha' - \alpha| + |\delta' - \delta|) \le 10^{-6}$. This calculation was performed thousands of times (at least 100.000 times) for each equation in the phase calculation. It was generated at least 99.999% of the time with an accuracy of 10^{-6}. The mathematical model of Eq. (19) was successfully tested until *Step* and N equal 1801, the value at which the increment $\Delta\theta$ would be 0.05°. Thus, it was believed that the chances for the equations to be wrong or false have been minimized.

https://doi.org/10.1017/jmech.2015.20 Published online by Cambridge University Press

4. BEFORE UNWRAPPING, CHANGE TO [–π, π]

Because of the character of the evaluation equations, only phase values $\alpha \in [0, \pi/4]$ and $\delta \in [0, \pi/2]$ radians were calculated. For unequivocal determination of the wrapped phase value angles $\in [-\pi, \pi]$ it was necessary to test values δ, $-\delta$, $\delta - \pi$, and $-\delta + \pi$ by combining them with α, $-\alpha$, $\alpha - \pi$, and $-\alpha + \pi$ using values of I_j and small systems in Eq. (30). The values were tested based on the symmetries of the tangent function. Sixteen tests are performed, and the correct values of α and δ are sought between $-\pi$ and π because the experimental values I_j and θ_j are known [12].

$$\begin{cases} I_1 = K\left[1-\cos(2\theta_1)\cos(\delta)-\cos(2\alpha)\sin(2\theta_1)\sin(\delta)\right] \\ I_2 = K\left[1-\cos(2\theta_2)\cos(\delta)-\cos(2\alpha)\sin(2\theta_2)\sin(\delta)\right] \\ \quad\cdots \\ I_N = K\left[1-\cos(2\theta_N)\cos(\delta)-\cos(2\alpha)\sin(2\theta_N)\sin(\delta)\right] \end{cases} \tag{30}$$

We obtain α and δ between $[-\pi, \pi]$. The next step is to unwrap the phase map. When unwrapping, several of the phase values should be shifted by an integer multiple of 2π. Unwrapping is thus adding or subtracting 2π offsets at each discontinuity encountered in the phase data. The Fig. 5 shows the wrapped phase map. The unwrapping procedure consists of finding the correct field number for each phase measurement [13,14].

Once obtained the value of α and δ unwrapping, applies digital implementation of the shear difference technique for whole field stress separation of 2-D problems of any geometry showed in [15-17]. Thus, it calculates the values of the phase maps, principal tensions (σ_1, σ_2) and normal (σ_x, σ_y) and shear (τ_{xy}) stresses. The von Mises stress or equivalent tensile stress (σ_v), a scalar stress value that can be computed, too. Thereafter, graphical displays of tensions in the object under study are shown.

5. TESTING AND ANALYSIS OF ERROR

To assess the practical use of the method developed in this work, a stress disk under diametric compression, D = 100.0mm in diameter, H = 5.0mm thick and made of epoxy, is used. The pixel numbers, which are used for digitization, are 1024 × 1024. The grey level of each pixel ranges from 0 to 255. The light source used in this experiment is white light from a sodium lamp. Figure 6 shows diagram of the assembly of experiments with the polariscope where only the analyzer is rotated (change the angle on each photo). Flowchart of processing applied to phase-shifting method in digital photoelasticity is show in the Fig. 7.

The Fig. 8 show isochromatic fringe orders of the experimental solution with new method. The fringe orders (n) are calculated by Eq. (31). Note in the picture, the presence of noise and defects due to imperfections of the photographs taken of the photoelastic model. Several sources of errors and uncertainties in photoelastic experiments are cited in [18].

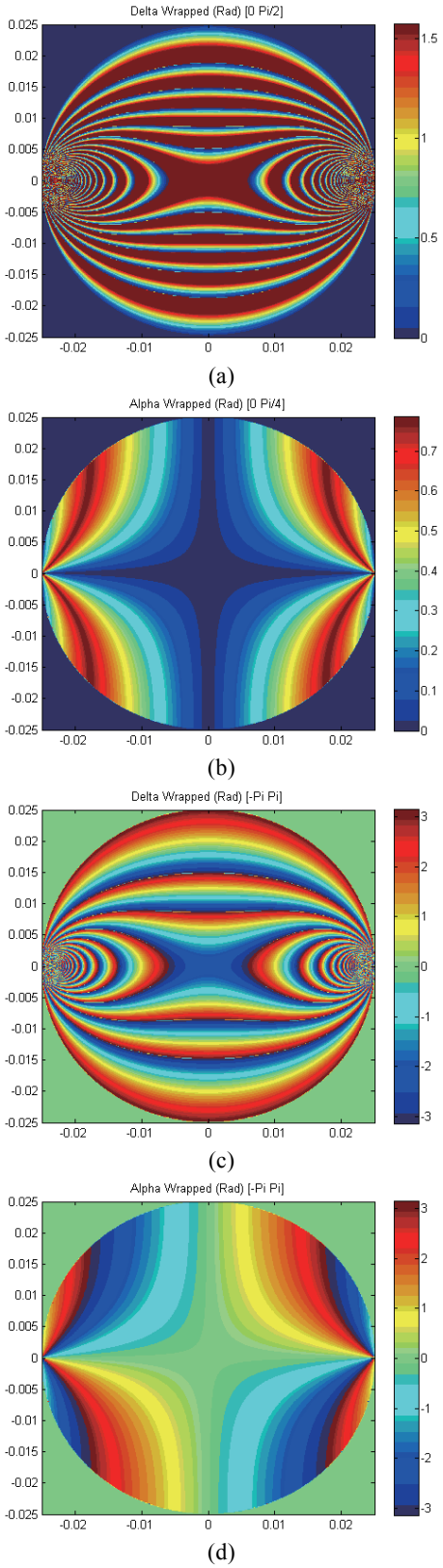


Fig. 5 The wrapped phase map: (A) isochromatic value (δ) obtained with the new equations with values between 0 and $\pi/2$, (B) isoclines angle (α) obtained with the new equations with values between 0 and $\pi/4$, (C) isochromatic value (δ) ready for unwrapping algorithm with values between $-\pi$ and π, (D) isoclines angle (α) ready for unwrapping algorithm with values between $-\pi$ and π.

https://doi.org/10.1017/jmech.2015.20 Published online by Cambridge University Press

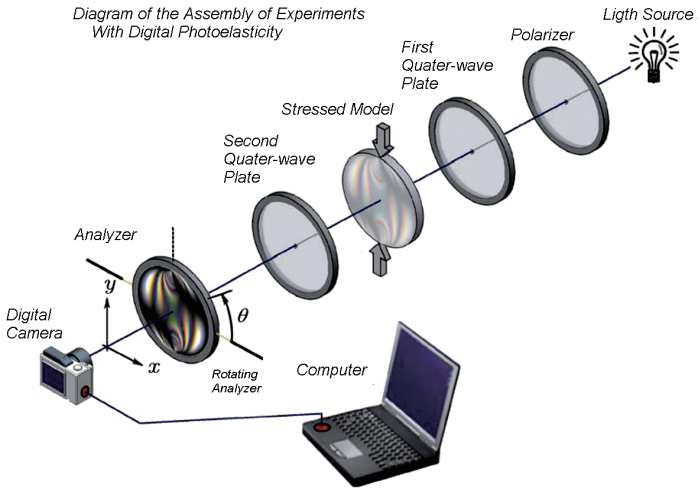


Fig. 6 Arrangement of the experiments (circular polariscope) with the new method proposed.

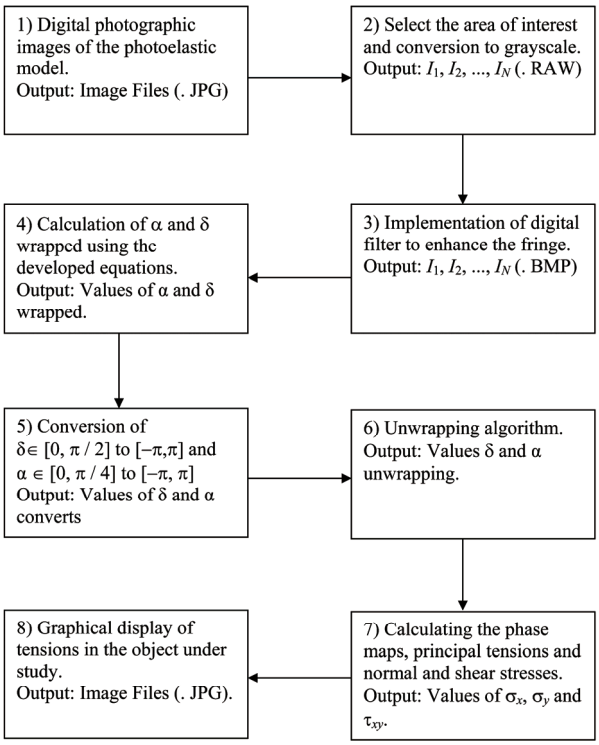


Fig. 7 Flowchart of processing with the outputs and results of each stage.

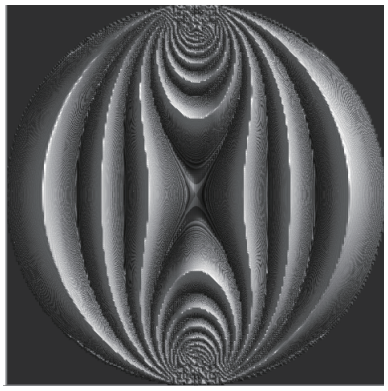


Fig. 8 Fringe orders (n) obtained from experimental measurements.

$$n = \frac{H}{F}(\sigma_1 - \sigma_2) \tag{31}$$

To test the new equations for the phase calculation, they were used with the technique of photoelasticity for an object with known stress and to evaluate the average error using Eqs. (32) and (33). This process was started with three images, repeated with four, then five and so on. The idea was to show that with an increasing number of images, the average error tends to decrease. Figure 9 shows an example of this procedure by 6 images.

$$Average \quad Error \quad for \quad \alpha \quad (E_\alpha) = \frac{1}{M}\sum_{i=1}^{M}\frac{|\alpha_i^e - \alpha_i|}{|\alpha_i^e|} \tag{32}$$

$$Average \quad Error \quad for \quad \delta \quad (E_\delta) = \frac{1}{M}\sum_{i=1}^{M}\frac{|\delta_i^e - \delta_i|}{|\delta_i^e|} \tag{33}$$

where M is the number of pixels of the image ($M = 1.048.576$) and α_i^e and δ_i^e are the exact value calculated by Eqs. (6) ~ (12) for the disk. The values of α_i and δ_i are calculated by the new equation. In the analysis of the error, only the zones within the photos that were unambiguous and contained no inconsistencies were considered [19].

Figure 10 show the results obtained with the application of the new phase calculation equations developed for a values of N and *Step*. There is not visual or graphic difference between the results obtained using different equations. This is due to high resolution graphics of photographic images, and the good results achieved with the new equations developed in the research. Numerically, the equations with more images have less uncertainty and therefore they are more accurate. Thus there was obtained the best values of stress with number of images $N = 31$ and $Step = 31$, than using $N = 3$ and $Step = 3$.

To compare the new equations for calculating the phase, nine sets of photos with *Step* set to 3, 4, 6, 7, 10, 11, 16, 19, and 31 were generated. In each set, the angle θ of the analyzer is varied ($\Delta\theta$): 45°, 30°, 18°, 15°, 10°, 9°, 6°, 5°, and 3°, respectively. Each set was computed using the average error of 3 to the number of *Step* images and using equations to evaluate the angles α and δ. Figures 11 and 12 show that the average error decreases when the number of images increases. It may be noted that for a number of images, the average error increases when the variation of the angle θ between the images decreases.

It is important to note that for each equation developed, the average errors found for the angle δ are larger than the errors found for the angle α of the fringes isoclines. It is believed that this occurs because the absolute values of δ are higher than the absolute values of α.

To compare the phase calculation equations deduced this article with the equations deduced by other authors, the equations were applied to the analysis of error in the algorithm of Patterson and Wang [21]. Values of $E_\alpha = 2104 \times 10^{-6}$ rad and $E_\delta = 5312 \times 10^{-6}$ rad were obtained.

https://doi.org/10.1017/jmech.2015.20 Published online by Cambridge University Press

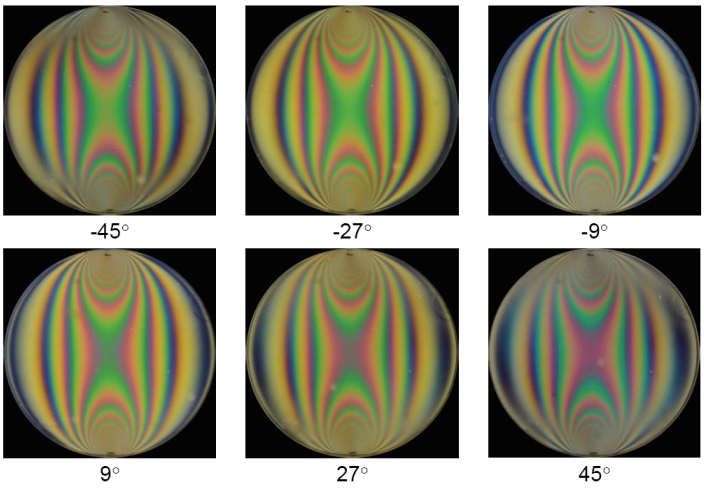


Fig. 9 Set with 6 images, $\Delta\theta$ equal to 18°, the disk is under compression.

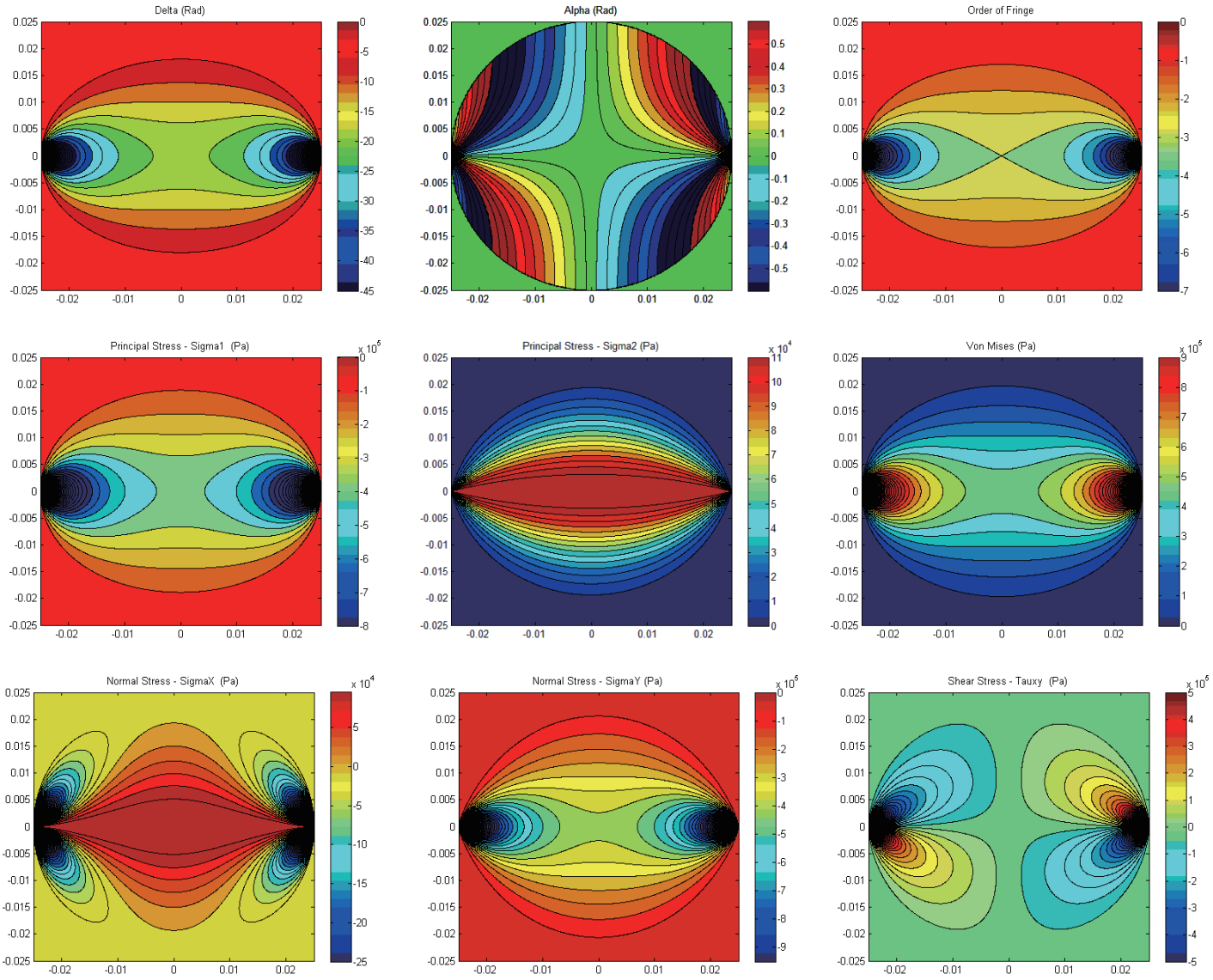


Fig. 10 Results obtained through experimental measurements using the new equations with $N = 19$ and $Step = 10$ of δ, α, fringe order(n), σ_1, σ_2, von Mises stress(σ_υ), σ_x, σ_y and τ_{xy}.

https://doi.org/10.1017/jmech.2015.20 Published online by Cambridge University Press

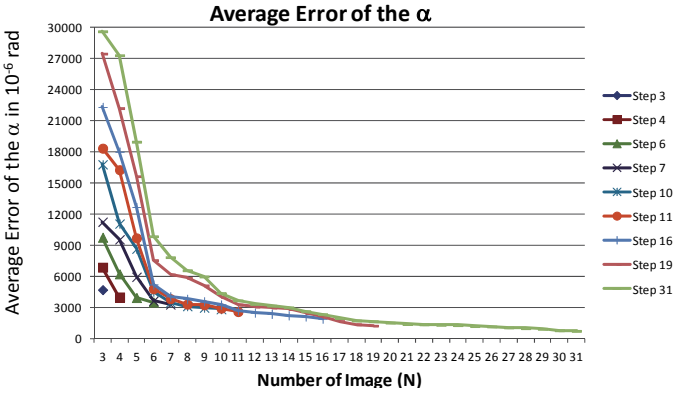


Fig. 11 A plot of the data with the average error in 10^{-6} rad versus the number of frames (N) for angle α.

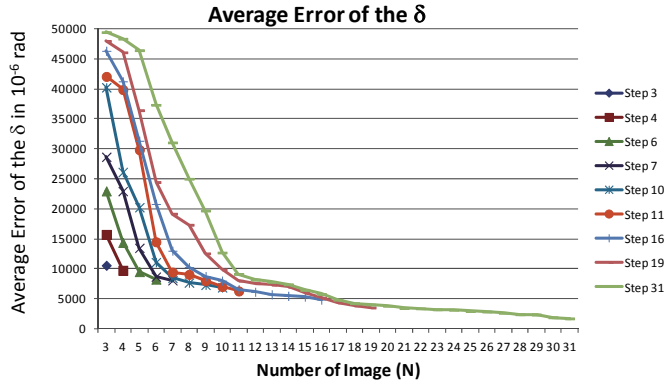


Fig. 12 A plot of the data with the average error in 10^{-6} rad versus the number of frames (N) for angle δ.

For the Patterson and Wang algorithm with six images, the average error is less than six images using the new equations. It is believed that the major distinction between the pictures of the phase shifts is the reason why this improved result is obtained. However, to obtain these images, it is necessary to rotate the analyzer and the second plate of the polariscope by a quarter wave.

The average error of the algorithm of Wang and Patterson with 6 images is in the range of the average error found for 11 images using the new equations, but for more than 16 images, lower average errors for the newly developed equations can be observed, indicating than a larger number of images yielded smaller errors. Similar results were obtained with the algorithms proposed by other authors in [22-26].

More experiments were performed with other values of load (P), diameter of the disk (D), the disk thickness (H), and material fringe constant (F) with very similar results. These new experiments were conducted to validate and confirm the proposed method.

6. CONCLUSIONS

This paper addresses the equations used for phase calculation measurements with images using phase shifting technique. The new equations are shown to be capable of processing the optical signal of photoelasticity. These techniques are very precise, easy to use, and low cost. On the basis of the performed error analysis, it can be concluded that the new equations are very good phase calculation algorithms. The metric analysis of the considered system demonstrated that its uncertainties of measurement depend on the frame period of the grid, on the resolution of photos in pixel and on the number of frames. However, the uncertainties involved in the measurement of the geometric parameters and the phase still require attention. In theory, if we have many frames, the measurement errors become very small. The measurement results obtained by the optical system demonstrate its industrial and engineering applications in experimental mechanics.

New numerical equations are deduced to calculate the directions of the tensions and delays (phase maps of the isoclines and isochromatic fringes) for the full-field image automatically, by programming the phase shift method in digital photoelasticity. With these new equations, a larger number of images phase shifted only by rotation of the analyzer can be used, and the gain can be calculated with lower uncertainties. Numerical methods were employed in an unprecedented way with the photoelastic technique to obtain a methodology for deriving the new equations. Until now, these equations were determined by algebraic and analytic methods.

With the new equations, it was possible to develop a photoelastic system that moves the analyzer of the polariscope at a constant speed while a camera takes many pictures at equal intervals of times, like a film. The camera must have a very short exposure time (high shutter speeds). With this technique, the obtained measurements are more precise, and there are fewer uncertainties.

Digital photoelasticity is an important optical metrology follow-up for stress and strain analysis using full-field digital photographic images. Advances in digital image processing, data acquisition, procedures for pattern recognition and storage capacity enable use of the computer-aided technique in automation and facilitate improvement of the digital photoelastic technique. Photoelasticity has seen some renewed interest in the past few years with digital imaging, image processing and new methods becoming readily available. However, further research is needed to improve the accuracy, the precision and the automation of the photoelastic technique.

ACKNOWLEDGMENTS

The authors thank the generous support of the Pontificia Universidade Catolica de Minas Gerais – PUCMINAS, the Conselho Nacional de Desenvolvimento Cientifico *e* Tecnologico - CNPq – "National Counsel of Technological and Scientific Development" and Fundacao de Amparo a Pesquisa de Minas Gerais – FAPEMIG – "Foundation for Research Support of Minas Gerais".

https://doi.org/10.1017/jmech.2015.20 Published online by Cambridge University Press

REFERENCES

1. Asundi, A. K., *MATLAB for Photomechanics — A Primer*, Elsevier Science, p. 67 (2002).
2. Asundi, A. K., Tong, L. and Boay, C. G., "Determination of Isoclinic and Isochromatic Parameters Using the Three-Load Method," *Measurement Science and Technology*, **11**, pp. 532–544 (2000).
3. Ramesh, K., "Digital Photoelasticity," *Measurement Science and Technology*, **11**, p. 1826, doi:10.1088/0957-0233/11/12/704 (2000).
4. Chen, T. Y., Lee, H. L. and Chou, Y. C., "An Improved Two-Load Method for Whole-Field Complete Photoelastic Fringe Analysis," *Journal of Mechanics*, **21**, pp. 199–203, doi: http://dx.doi.org/10.1017/S1727719100000630 (2005).
5. Yao, X. F., Jian, L. H., Xu, W., Jin, G. C. and Yeh, H. Y., "Digital Shifting Photoelasticity with Optical Enlarged Unwrapping Technology for Local Stress Measurement," *Optics & Laser Technology*, **37**, pp. 582–589 (2009).
6. Chang, C. W., Chen, P. H. and Lien, H. S., "Separation of Photoelastic Principal Stresses by Analytical Evaluation and Digital Image Processing," *Journal of Mechanics*, **25**, pp. 19–25, doi: http://dx.doi.org/10.1017/S1727719100003567 (2009).
7. Baek, T. H., Kim, M. S., Morimoto, Y. and Fujigaki, M., "Separation of Isochromatics and Isoclinics from Photoelastic Fringes in a Circular Disk by Phase Measuring Technique," *KSME International Journal*, **16**, pp. 175–181 (2002).
8. Collett, E., *Field Guide to Polarization*, SPIE Press, Bellingham, Washington, U.S. (2005).
9. Ng, T. W., "Derivation of Retardation Phase in Computer-Aided Photoelasticity by Using Carrier Fringe Phase Shifting," *Applied Optics*, **36**, pp. 8259–8263 (1997).
10. Oh, J. T. and Kim, S. W., "Polarization-Sensitive Optical Coherence Tomography for Photoelasticity Testing of Glass/Epoxy Composites," *Optics Express*, **11**, pp. 1669–1676 (2003).
11. Magalhaes, P. A. A., Neto, P. S. and Barcellos, C. S., "Analysis of Shadow Moire Technique with Phase Shifting Using Generalisation of Carre Method," *Strain*, **47**, pp. e555–e571, doi: 10.1111/j.1475-1305.2009.00655.x (2011).
12. Arellano, N. I. T., Zurita, G. R., Fabian, C. M. and Castillo, J. F. V., "Phase Shifts in the Fourier Spectra of Phase Gratings and Phase Grids: An Application for One-Shot Phase-Shifting Interferometry," *Optics Express*, **16**, pp. 19330–19341 (2008).
13. Estrada, J. C., Servin, M. and Quiroga, J. A., "Noise Robust Linear Dynamic System for Phase Unwrapping and Smoothing," *Optics Express*, **19**, pp. 5126–5133 (2011).
14. Navarro, M. A., Estrada, J. C., Servin, M., Quiroga, J. A. and Vargas, J., "Fast Two-Dimensional Simultaneous Phase Unwrapping and Low-Pass Filtering," *Optics Express*, **20**, pp. 2556–2561 (2012).
15. Ramji, M. and Ramesh, K., "Whole Field Evaluation of Stress Components in Digital Photoelasticity — Issues, Implementation and Application," *Optics and Lasers in Engineering*, **46**, pp. 257–271 (2008).
16. Ramji, M. and Ramesh, K., "Stress Separation in Digital Photoelasticity, Part A — Photoelastic Data Unwrapping and Smoothing," *Aerospace Science and Technology*, **60**, pp. 5–15 (2008).
17. Ramji, M. and Ramesh, K., "Stress Separation in Digital Photoelasticity, Part B — Whole Field Evaluation of Stress Components," *Aerospace Science and Technology*, **60**, pp. 16–25 (2008).
18. Pinit, P. and Umezaki, E., "Digitally Whole-Field Analysis of Isoclinic Parameter in Photoelasticity by Four-Step Color Phase Shifting Technique," *Optics and Laser in Engineering*, **45**, pp. 795–807 (2007).
19. Ashokan, K. and Ramesh, K., "Finite Element Simulation of Isoclinic and Isochromatic Phasemaps for Use in Digital Photoelasticity," *Experimental Techniques*, **33**, pp. 38–44 (2009).
20. Ramesh, K., *Digital Photoelasticity: Advanced Techniques and Applications*, Springer-Verlag, Berlin, Germany, pp. 165–178 (2000).
21. Patterson, E. A. and Wang, Z. F., "Towards Full Field Automated Photoelastic Analysis of Complex Components," *Strain*, **27**, pp. 49–57 (1991).
22. Ramji, M. and Prasath, R. G. R., "Sensitivity of Isoclinic Data Using Various Phase Shifting Techniques in Digital Photoelasticity Towards Generalized Error Sources," *Optics and Lasers in Engineering*, **49**, pp. 1153–1167 (2011).
23. Chang, S. H. and Wu, H. H. P., "Improvement of Digital Photoelasticity Based on Camera Response Function," *Applied Optics*, **50**, pp. 5263–5270 (2011).
24. Ajovalasit, A., Petrucci, G. and Scafidi, M., "RGB Photoelasticity Applied to the Analysis of Membrane Residual Stress in Glass," *Measurement Science and Technology*, **23**, p. 025601, doi:10.1088/0957-0233/23/2/025601 (2012).
25. Buckberry, C. and Towers, D., "Automatic Analysis of Isochromatic and Isoclinic Fringes in Photoelasticity Using Phase Measuring Techniques," *Measurement Science and Technology*, **6**, p. 1227 doi:10.1088/0957-0233/6/9/ 001 (1995).
26. Quiroga, J. A. and Cano, A. G., "Automatic Determination of Isostatics in Two-Dimensional Photoelasticity," *Measurement Science and Technology*, **11**, p. 259, doi:10. 1088/0957-0233/11/3/313 (2000).

(Manuscript received September 13, 2012, accepted for publication January 13, 2015.)

https://doi.org/10.1017/jmech.2015.20 Published online by Cambridge University Press